
Oral presentation | Reacting flow

Reacting flow

Tue. Jul 16, 2024 2:00 PM - 3:30 PM Room D

[5-D-02] Influence of low-temperature chemistry modelling on flame characteristics in a ducted rocket combustor

*Niklas Zettervall¹, Christian Ibron¹, Kevin Nordin-Bates¹ (1. Swedish Defence Research Agency, FOI)

Keywords: Reduced chemical kinetics, Ducted rocket, Propane, Low-temperature modelling, Ignition delay time

Influence of low-temperature chemistry modelling on flame characteristics in a ducted rocket combustor

N. Zettervall, C. Ibron and K. Nordin-Bates

Corresponding author: niklas.zettervall@foi.se

Swedish Defence Research Agency, Stockholm, Sweden

Abstract: With the increase in computational capacities reactive Computational Fluid Dynamics (CFD) is becoming more feasible and affordable. Cases that were unrealistic to simulate just a decade ago can now benefit from the improvements gained by high-fidelity combustion simulations. A key component in all combustion cases is the modelling of the chemistry, where the chemical kinetics is modelled using a reaction mechanism consisting of between one and many thousands of reaction depending on the degree of chemical complexity added. In this study a ramjet combustor, a Ducted Rocket is simulated using four different reaction mechanisms, each representing a level of chemical complexity. Presented in this study is a novel reduced reaction mechanism that incorporates low-temperature chemistry modelling. The CFD simulations shows that the results when using the novel mechanism, with its low-temperature chemistry modelling, is similar to those of the CFD simulation using the detailed reaction mechanism, indicating that improved chemistry modelling is a key part when simulation the Ducted Rocket case.

Keywords: Ducted Rocket, Ramjet, Large Eddy Simulation, Finite-Rate Chemistry, Chemical Kinetics, Reduced Mechanisms

1 Introduction

Ramjet engines provide economical air-breathing propulsion systems at medium to high Mach numbers, with areas of application including transportation, reusable launch vehicles and hypersonic cruise missiles [1]. Solid, liquid and gaseous fuels can be used for propulsion, providing high fuel flexibility. A fourth option, possible for use in engine test beds, is to use a surrogate gas fuel prior to entering the combustor, to enhance the fuel-air mixing, shortening the time to ignition and stable combustion.

Computational Fluid Dynamics, CFD, is a key tool for investigating and improving ramjet combustors. Here the flow modelling is coupled tightly to the modelling of chemical processes in the system. The finite-rate approach for chemistry modelling uses an explicit reaction mechanism to model the rate of production and consumption of individual species in the flow. Such a mechanism consists of a number of reactions, each with a corresponding reaction rate. This mechanism is combined with modelling of the thermodynamics and transport of the individual species to give a reactive flow system that can capture key flame parameters such as the laminar flame speed, flame temperature and ignition delay times.

In a ramjet combustor, the high flow speeds and hence short time scales mean that the modelling of the ignition delay time needs to be accurate over a wide range of temperatures and pressures in order to accurately capture the position and anchoring points of a flame. For n-alkane hydrocarbons with five carbons or more, the low-temperature ignition characteristics are associated with an increasing ignition time as the temperature rises before, at sufficiently high temperatures, the ignition time starts to decrease again. This phenomena, known as the Negative Temperature Coefficient behavior, NTC [2], occurs from roughly 600 K up to 1000 K depending on initial gas pressure. Smaller alkanes, such as propane, can have a similar but

less pronounced ignition behavior at low temperatures, and capturing this ignition characteristic in the modelling can be a challenge.

This study investigates numerically a research ramjet combustor from ONERA [3]. Several studies of the combustor, investigating both cold and hot flow, have been performed over the years [3–5]. The combustor can be operated with either liquid fuel or, as is used here, using gaseous propane fuel simulating a pre-vaporized solid fuel.

Large Eddy Simulation (LES) computations of the reactive flow in the combustor at $0.5 \leq \phi \leq 0.75$ have previously been presented in [5]. These computations used a Smagorinsky turbulence model and Thickened Flame combustion model together with a one-step chemistry scheme for propane combustion. Results at $\phi=0.5$ were compared with experimental measurements along a number of $y=0$ and $z=0$ centerlines of the combustor. Results at $\phi=0.75$ demonstrated a strong periodic behavior. In the paper by Roux et al. [6], reacting LES with a single-step chemistry were carried out for $\phi=0.5$ and 0.75 equivalence ratios. Spectral analysis of pressure signals together with Proper Orthogonal Decomposition (POD) was employed to analyze the unsteady modes in the reacting LES. These identified a number of strong transverse modes and a weak longitudinal mode.

This study combines both novel modelling of the reaction kinetics of propane (with low-temperature chemistry included) and combustion LES of the Ducted Rocket combustor. In order to investigate the influence of the chemical modelling on the LES predictions, four different reaction mechanisms, ranging from global to detailed, are simulated. Two of the reaction mechanisms lack low-temperature chemistry, where one predicts excessively fast ignition times whereas the other predicts a time to ignition that is too long compared to experimental data. The novel mechanism presented here, along with a highly chemically complex and computationally expensive mechanism, both include low-temperature chemistry, spanning a wide range of temperatures and pressures where the correct ignition characteristic can be modelled. The influence of the low-temperature chemistry in the reaction mechanisms on the overall results of the LES is investigated by analyzing combustor mean fields, flame anchoring positions and pressure fluctuations.

2 ONERA Ducted Rocket Combustor

The ducted rocket experimental rig developed at ONERA [3] was designed to provide a simple set-up for the study of ramjet combustion and validation of numerical codes. It simulates experimentally a Solid-propellant Ducted Rocket (SDR) motor, in which solid propellant is used to generate partially burned product gases, which are then injected into a main combustor where they burn aerobically. In the experimental rig, gaseous propane is used to represent these gas generator products.

As illustrated in Figure 1, the engine is based upon a rectilinear combustion chamber of square cross-section $100 \times 100 \text{ mm}^2$ and length 1020 mm. This is fed with gaseous propane fuel at its head by two circular inlets of diameter 11 mm. Air is introduced into the chamber via two opposing ducts with square cross-section $50 \times 50 \text{ mm}^2$, entering at an angle of 45° . At the exit of the combustion chamber, a convergent choked nozzle with minimum cross section $100 \times 55.8 \text{ mm}^2$ accelerates the products before they leave the engine at supersonic speeds. The air inlet ducts extend 900 mm upstream of the combustion chamber, terminating in shocked inlet nozzles with a minimum cross-sectional area of 468 mm^2 . Note that some inconsistency in the description of the combustor is introduced in subsequent publications, in particular the exit nozzle dimensions and the length of the uniform section of the combustion

chamber. Here, the dimensions are taken from the original experimental paper of Ristori et al. [4].

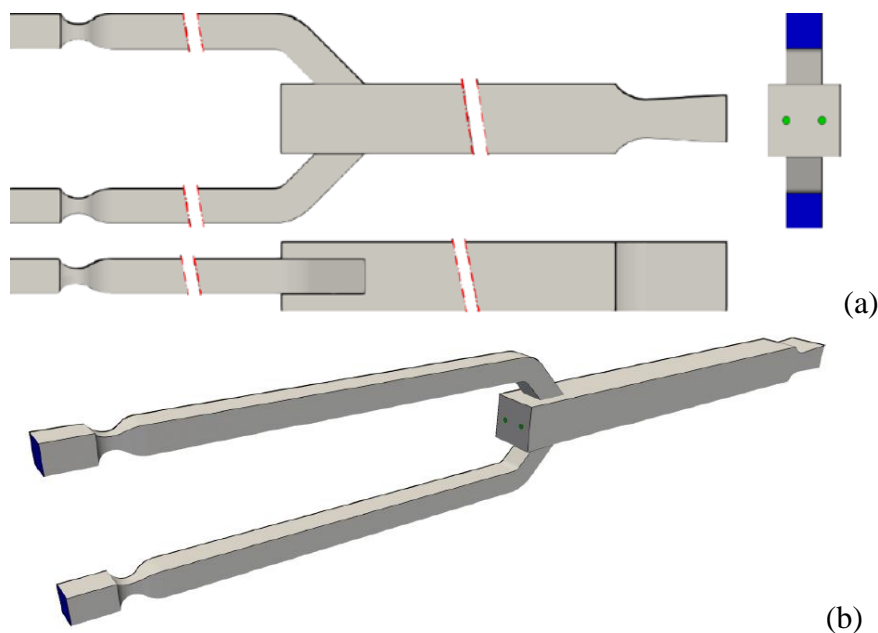


Figure 1: Ducted rocket internal geometry. Side, rear and top in (a), and perspective view in (b). Blue surfaces show air inlet boundaries, green surfaces fuel inlets.

Three sets of inflow conditions have been presented in the literature, representative of low, medium and high altitude flight. This study focuses on the high altitude conditions with an air mass flow rate of 0.9 kg/s and air inlet total temperature of 750 K. The fuel mass flow is varied to achieve the desired overall equivalence ratio. In this study the medium speed case is considered, corresponding to an equivalence ratio of $\phi = 0.5$. Table 1 shows the three flight conditions, highlighting the medium speed case studied here.

Table 2: Case configurations: global equivalence ratio, inlet mass flow rate and total temperature for propane fuel and air respectively

Flight condition	ϕ	$\dot{m}_{C_3H_8}$ [kg/s]	T_{fuel} [K]	\dot{m}_{air} [kg/s]	T_{air} [K]
Low speed	0.35	0.020	750	0.90	350
Medium speed	0.50	0.029	750	0.90	350
High speed	0.75	0.044	750	0.90	350

3 Reaction mechanism development

The development of the novel reaction mechanism presented here, called Z87 (with the number corresponding to the number of reactions in the mechanism), follows the same methodology [7] as used when developing the previously presented propane mechanism, Z66 [8]. This methodology has also produced reduced reaction mechanisms for a range of other hydrocarbon fuels [9-13]. The methodology divides the chemistry into three subsections: *Fuel breakdown*, *Intermediate hydrocarbons* and *Base mechanism*. The main difference

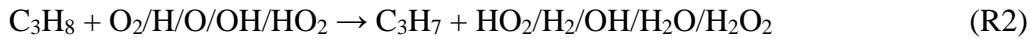
between the previously presented Z66 mechanism and the novel Z87 is that the latter includes improved modelling of the low-temperature chemistry, enhancing the modelling capability of ignition delay times below approximately 1000 K.

Details of the development methodology have been extensively tested and presented previously [7,9,14] hence the Base mechanism and Intermediate hydrocarbon subsections will not be presented in any detail here. In short, the Base mechanism contains most of the key radical chemistry, and includes species in the H₂-O₂ and C₁-O₂ chemistries. Due to the significance of these chemistries on the overall oxidation process, the Base mechanism is modelled in more detail compared to the other two subsections. The Intermediate hydrocarbon subsection, responsible for the C₂ chemistry, acts as a bridge between the Fuel breakdown subsection and Base mechanism, and the reduction of species and reactions in this subsection is significant.

The main difference between Z66 and Z87 lies in the extent of the low-temperature modelling, and the additional modelling of Z87 over Z66 is present in the Fuel breakdown subsection. Where Z66 decomposed the propane fuel into C₁ and C₂ species using only two reactions, Z87 instead oxidizes the fuel into both C₁ and C₂ but also C₃ radical species such as C₃H₇ and C₃H₆. Treating the fuel breakdown in a more chemically correct manner means that the mechanism is capable of accurately predict ignition delay times over a wider range of temperatures. The propane fuel in Z87 can be thermally decomposed via



or it can undergo H-abstraction using any of the five reactions, shown in compressed format in reactions R2, where the propane reacts with either O₂, H, O, OH or HO₂, creating a propyl radical (C₃H₇) and HO₂, H₂, OH, H₂O or H₂O₂, respectively.



The propyl radical is either decomposed using fall-off reactions, creating C₂H₄ and CH₃, or C₃H₆ and H, or it reacts with O₂ creating either C₃H₆ or C₃H₆OOH. The C₃H₆ radical in turn is decomposed, producing C₂H₃ and CH₃, or oxidized via H, O or OH, producing C₂ and C₁ species. C₃H₆OOH on the other hand continues the O₂-addition, creating OC₃H₅OOH and a hydroxyl radical (OH). This last reaction pathway resembles the one in the oxidation of larger n-alkanes [15,16] where a two-stage O₂-addition eventually forms a hydroxyl radical which in turn increases the low-temperature reactivity. It is key to capture this reaction pathway if a correct low-temperature ignition characteristic is to be modelled, hence, it is impossible for global or overly simplified reduced reaction mechanisms to capture accurately these characteristics due to the lack of this reaction pathway.

Overall, the Fuel breakdown subsection consists of 20 reactions forming complex reaction pathways where the propane fuel and its radical species can both thermally decompose or fully oxidize all the way to smaller C₁ species. This complex set of Fuel breakdown reactions manages to capture key reaction pathways where different pathways are dominating in different temperature ranges, yet doing so using a highly compressed set of reactions. All other reaction mechanisms capable of this level of modelling accuracy consists of hundreds or thousands of more reactions, making them too expensive for CFD and finite-rate LES in particular. In total, the Z87 mechanism consists of 30 species and 87 reactions, out of which 15 reactions are reversible.

3.1 Mechanism validation

The validation of Z87 includes simulations of the laminar flame speed, s_L , the maximum flame temperature, T_{max} , and the ignition delay time, τ_{ig} , the latter for a wide range of

different initial gas temperatures and pressures. Z87 will be compared against one global reaction mechanism by Westbrook and Dryer [17], WD2, the Z66 mechanism, and two highly detailed mechanisms, the San Diego (SD) [18] and Aramco 3.0 [19] mechanisms. WD2, Z66, Z87 and SD mechanisms are then all used in the LES of the Ducted Rocket presented below. The Aramco 3.0 mechanism is one of the most chemically complex mechanisms for propane combustion modelling but is also too computationally expensive to use in LES.

The WD2 mechanism consists of only two reactions, converting propane into CO and H₂O in one reaction and in a second reaction CO into CO₂. It is obvious that such a simple chemical description will have modelling limitations, and all chemical details of radical formation, temperature and pressure dependencies and equivalence ratio flexibilities will be limited or absent. WD2 is however computationally significantly cheaper than almost all other reaction mechanisms present. The question one must ask however is if the poor modelling of the WD2 mechanism is too limiting.

The Z66 mechanism, consisting of 66 irreversible reactions, approaches the modelling in a completely different manner compared to WD2, and Z66 uses an accurate underlying H₂-O₂ and C₁-O₂ submechanism. This means that it will be capable of capturing key flame characteristics such as laminar flame speed, species profiles in the flame, radical formation, flame temperature and ignition delay times at higher temperatures. In many ways the modelling results resembles those predicted by significantly larger mechanisms but at a fraction of the computational cost. However, as previously mentioned the too simple description of the low-temperature chemistry in Z66 means that ignition characteristics at lower temperatures are not modelled correctly, and this is where the novel Z87 and the accompanying improved modelling resolves this issue.

The SD mechanism is a detailed mechanism, with 58 species and 270 reversible reactions. It is significantly more complex than the other three mechanisms, but compared to other detailed mechanisms, such as the Aramco 3.0 mechanism, it is significantly less chemically complex. As such, it also has a lower computational cost compared to most other detailed mechanisms, just low enough for it to be applicable in the present LES, but still too expensive for meshes with a higher number of cells.

3.2 Laminar flame speed

The laminar flame speed simulations are performed for a range of equivalence ratios, from $\phi = 0.5$ to $\phi = 1.8$, and initial gas temperatures, $T = 300$ K to 650 K, and pressures, $p = 1$ to 10 atm. Figure 2 show the laminar flame speed for $T = 300$ K and $p = 1$ atm. A large number of experimental data is included and it is clear that Z87 matches the data well for all equivalence ratios. The Aramco 3.0 and Z66 mechanisms also matches the data well whereas the SD mechanism has a slight over-prediction at fuel lean conditions and a slight under-prediction at fuel rich. WD2 manages to sometimes predict the flame speed at fuel lean conditions but completely fail above stoichiometric conditions. The result for WD2 is common for global mechanisms [8] and highlights the need for more chemically complex reaction pathways when fuel rich conditions are present.

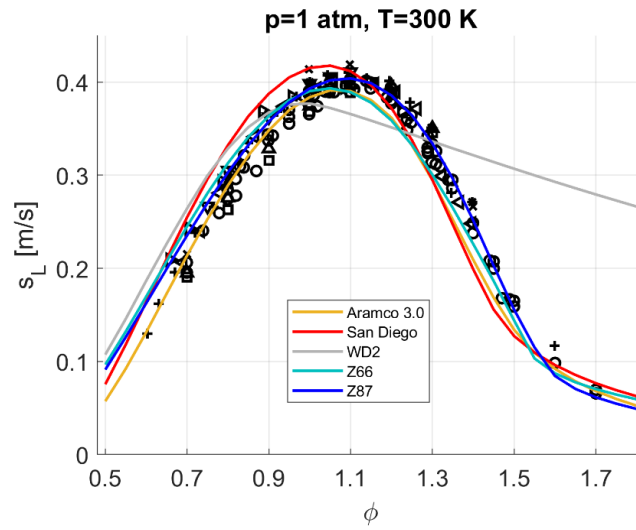


Figure 2: Laminar burning velocity at $p=1$ atm and $T=300$ K.
 Experimental data: [20–28]

At elevated initial gas temperatures, Figure 3, all mechanisms except WD2 match the experimental data well, with the same slight exception of the SD mechanism as seen in Figure 2. An increase in initial gas temperature of 73 K, Figure 3(a), results in an increase in flame speed by almost 50%, and at $T=650$ K, Figure 3(b), the flame speed is significantly elevated, reaching around 1.5 m/s. All mechanisms do, however, capture the increasing speeds seen when the initial temperature is increased. WD2 has the same trends at elevated temperatures as it has at 300 K, but even though its modelling is highly simplified, it manages to follow accurately the trend of the flame speed increases at fuel lean conditions. Z87 manages to capture the laminar flame speeds well across all initial gas temperatures.

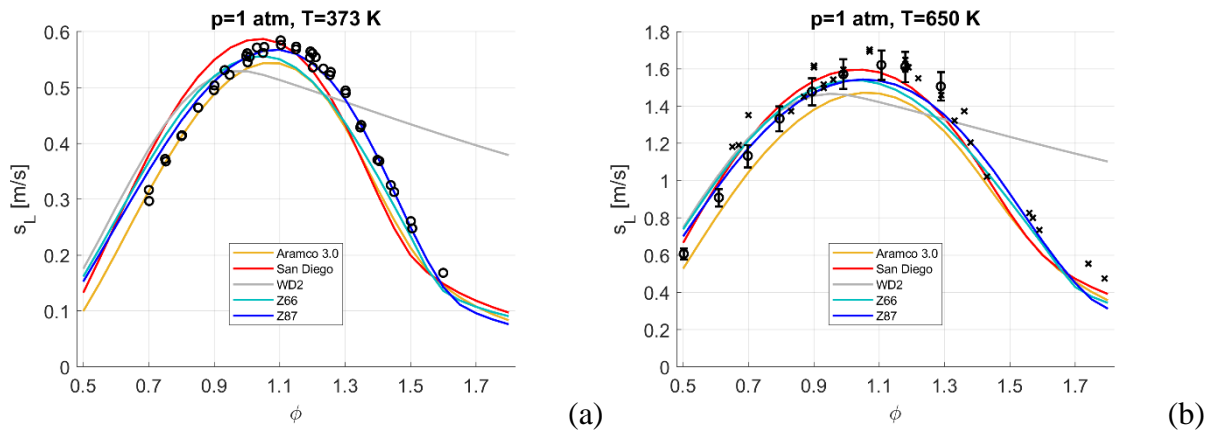


Figure 3: Laminar burning velocity at $p = 1$ atm and $T = 373$ K in (a) and $T = 650$ K in (b). Experimental data in (a): [20], and in (b): [24,29].

At elevated pressures of $p=5$ and 10 atm, Figure 4, the laminar flame speed modelled by the WD2 mechanism overpredicts the experimental data unlike the other mechanisms. A lack of pressure dependent third-body reactions in WD2 is the likely explanation for its poor modelling results. The other mechanisms do capture the correct trends of decreasing flame speeds with increasing pressures. At 5 atm, where there are experimental data, all mechanisms match the data reasonably, with Aramco 3.0 being the best at fuel lean conditions and Z66 and Z87 at fuel rich.

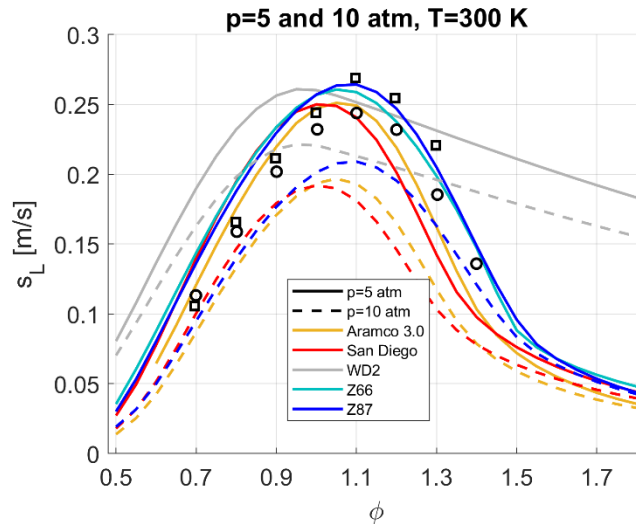


Figure 4: Laminar burning velocity at $p = 5$ atm and 10 atm, both at $T = 300$ K. Experimental data: [23,25].

Overall the modelling capabilities on the laminar flame speed using the Z87 mechanism is excellent, matching both detailed mechanisms and experimental data for a wide range of initial gas temperatures and pressures, and for a wide range of equivalence ratios.

3.3 Maximum flame temperature

The next flame characteristic investigated is the maximum flame temperature. In the one-dimensional domain, this temperature is present at the end of the domain, where exothermicity has peaked. Unsurprisingly the temperature is at its highest at around stoichiometric conditions, and all mechanisms show almost identical flame temperatures up to roughly $\phi=0.95$, after which the Z66 and WD2 have higher maximum temperature predictions compared to the other three mechanisms. The Z87, SD and Aramco 3.0

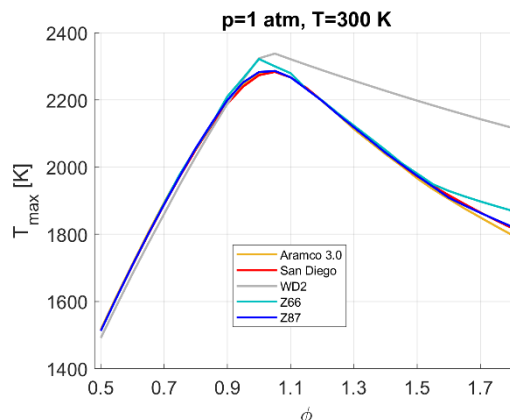


Figure 5: Maximum flame temperature.

mechanisms all give almost identical temperature predictions over the complete range of equivalence ratios.

3.4 Ignition delay time

The range of pressures for the evaluation of ignition delay time is dictated by availability of the experimental data. Note that all experimental data found in the open literature uses argon as a drive gas. This means that experimental data when using a shock tube, i.e. at higher temperatures, will result in longer ignition delay times than if air was used. However, since WD2, Z66 and Z87 do not include argon the best option was to simulate the ignition delay times using propane-air mixtures, keeping in mind that the high-temperature experimental data may show longer ignition times compared to the simulated values. In order to investigate the modelling accuracy of the detailed mechanisms, initial simulations using argon instead of air were made using both SD and Aramco 3.0. The results showed that both mechanisms matched the experimental data well, hence it was concluded that their modelling capacities were satisfactory and they could be used as reference mechanisms when using air instead of

Figure 5: Laminar flame temperatures at $p = 1 \text{ atm}$ and $T = 300 \text{ K}$.

argon. This means that WD2, Z66 and Z87 should primarily be compared against the detailed mechanisms at temperatures above roughly 1000 K . At temperatures below 1000 K a rapid compression machine is used in the experiments and in those cases the difference between using argon or air does not affect the experimental results. Hence, a direct comparison with those data points and the simulation results using air is acceptable.

At the lowest pressure simulated, $p = 1 \text{ atm}$ in Figure 6(a), it is immediately obvious that WD2 significantly under-predicts the ignition delay times, with times between one and two orders of magnitude faster compared to both the other mechanisms and the experimental data. Such fast ignition characteristics are common for global mechanisms and often results in [8] premature ignition in combustion CFD, potentially resulting in errors in the flame anchoring position. At this low pressure, there is only a weak fall-off of the ignition curve at lower temperatures. The Z66 mechanism, with its absence of a low-temperature chemistry, does start to deviate from the other three larger mechanisms below around 1100 K . At $p=6 \text{ atm}$, Figure 6(b), this trend is even greater, and at 1000 K the difference between Z66 and the other larger mechanisms is almost one order of magnitude. At an increased pressure, a fall-off of the ignition curve is clear. In both of these figures, Z87 is closely matching the predictions made by SD and Aramco 3.0.

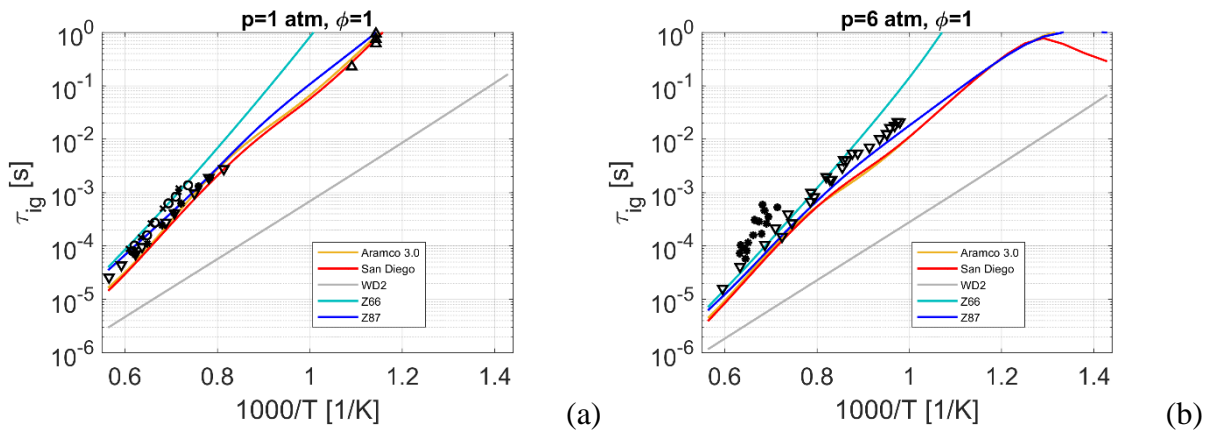


Figure 6: Ignition delay time at $\phi = 1.0$ and $p = 1$ atm in (a) and $p = 6$ atm in (b). Experimental data in (a): [28–31], and in (b): [30,32,33]

Increasing the pressure even further, to $p = 10$ atm in Figure 7(a) and $p = 20$ atm in Figure 7(b), further exaggerates the trends seen for the lower pressures. The fall-off of the ignition curve is highly visible, backed up by experimental data, and it is clear that at the lowest temperatures Z87 follows the highly chemically complex Aramco 3.0 mechanism closely. At these elevated pressures, the difference between the three largest mechanisms and Z66 is even greater than at the lower pressures, and WD2 continues to significantly under-predict the ignition times.

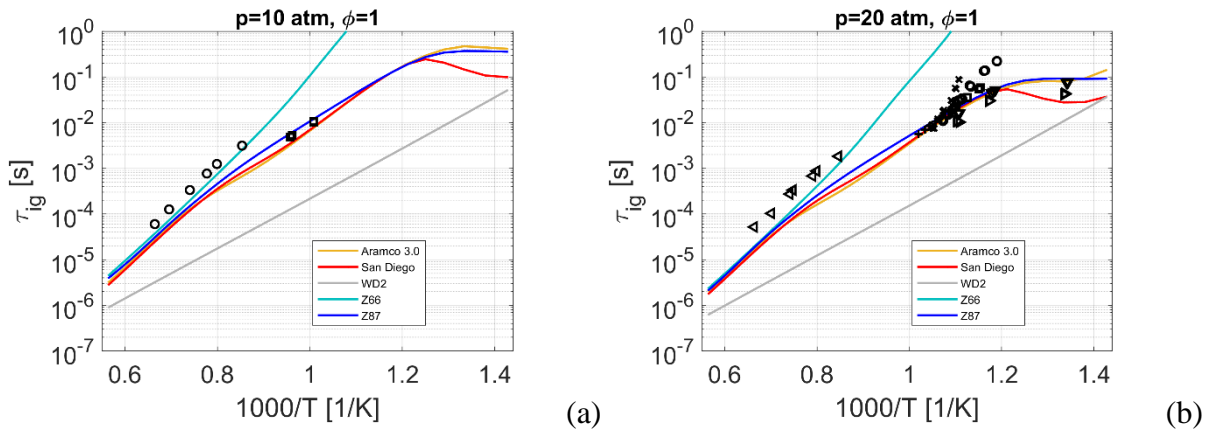


Figure 7: Ignition delay time at $\phi=1.0$ and $p=10$ atm in (a) and $p=20$ atm in (b). Experimental data in (a): [31,34], and in (b): [34–36].

Finally, at $p = 30$ atm in Figure 8(a), and $p = 55$ atm in Figure 8(b), the same trends as for the lower pressures continues. Note that the difference between WD2 and the three largest mechanisms continues to decrease as the pressure increases. The reason is that the ignition delay times predicted by the large mechanisms decreases, whereas this is not the case for WD2 to the same degree. This lack of pressure dependence of the WD2 mechanism was also seen in the laminar flame speeds presented above. The increase in pressure also exposes the poor low-temperature ignition capability of Z66, whose ignition curve has significantly deviated from the other mechanisms, at lower temperatures.

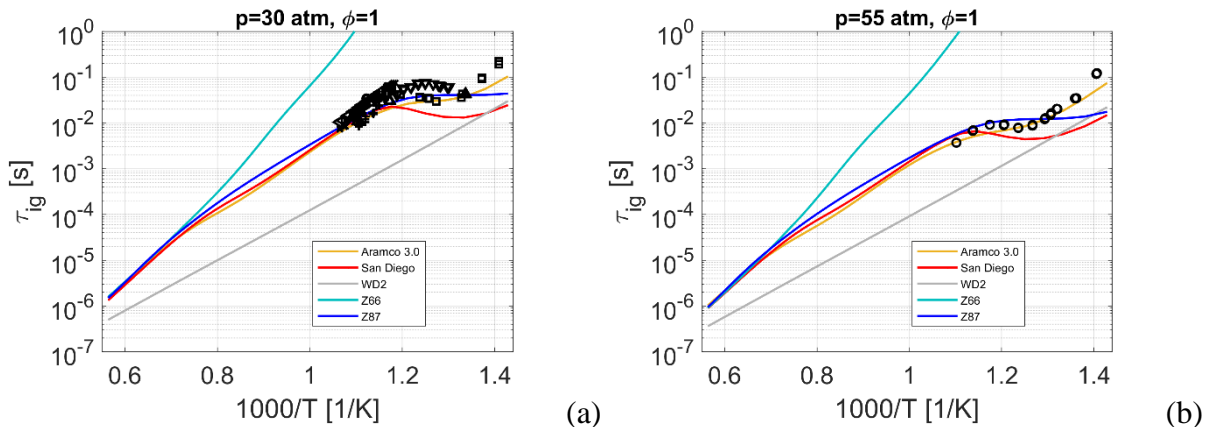


Figure 8: Ignition delay time at $\phi = 1.0$ and $p = 30$ atm in (a) and $p = 55$ atm in (b). Experimental data in (a): [34,35,37], and in (b): [37].

4 LES of ONERA Ducted Rocket

4.1 Methodology and set-up

In the following sections, the four reaction mechanisms are used in LES of the ONERA Ducted Rocket combustor. The reactive LES model, based on spatially filtered, unsteady, compressible transport equations for mass, momentum, energy and species mass fractions, uses filtered source terms to account for changes in composition and specific enthalpy due to chemical reactions, as well as for interactions between the resolved flow and the unresolved sub-grid scale motions. The governing equations are closed with constitutive equations for an ideal gas with Sutherland viscosity, Fourier heat conduction and Fickian diffusion [38]. Turbulent diffusivities for heat and mass are calculated from constant Prandtl and species individual Schmidt numbers, respectively. The source terms are closed using the Localized Dynamic k-equation Model (LDKM) [39]. Chemical reaction rates are computed using Arrhenius rate laws, which results in net production rates for individual species based on the law of mass-action [38]. The LES filtered reaction rate is modelled using the Partially Stirred Reactor (PaSR) model [40]. The PaSR model has been extensively tested and is validated for laboratory combustors [41,42], afterburners [8], gas turbine combustors [43] and different scramjet combustors [44,45]. Wall treatment in the combustor and air intake ducts includes isothermal walls at 600 K, and wall functions for turbulent viscosity, implemented from the standard OpenFOAM library. Local values of the dimensionless wall distance y^+ vary between 40 and 400 in both air intake ducts and the combustor duct.

The governing equations are discretized and solved using a semi-implicit finite-volume code based on the OpenFOAM C++ library [46]. The code is an extension of the reactingFoam solver, and is pressure-based, using a PISO-type algorithm. The chemical source terms in the system are evaluated using an operator-splitting approach together with an adaptive Rosenbrock solver for the resultant stiff system of ODEs [48].

Initial simulations ran on a mesh using 2.25 million cells, and based on the results from this mesh an improved mesh was generated. The refined grid used results from the coarse grid in order to target the refinement, specifically using results of the magnitude of the gradient of the velocity, the mean of the heat release and the mean of the fuel. This way the refinements are targeted to areas of the flame and fluid flow that benefit most from increased resolution. In practice this means that additional cells are concentrated on the walls of the incoming air jets, in the back of the combustor where the fuel is most present and in areas where the heat release, i.e. in the flame front, where most of the light fast-reacting species are most present. The resulting final mesh consists of 12.7 million hexahedra cells, with all four simulations using the exact same mesh in order to maximize consistency between the different cases. Figure 9 shows the mesh where the air inlets enter the combustor, in two levels of zoom.

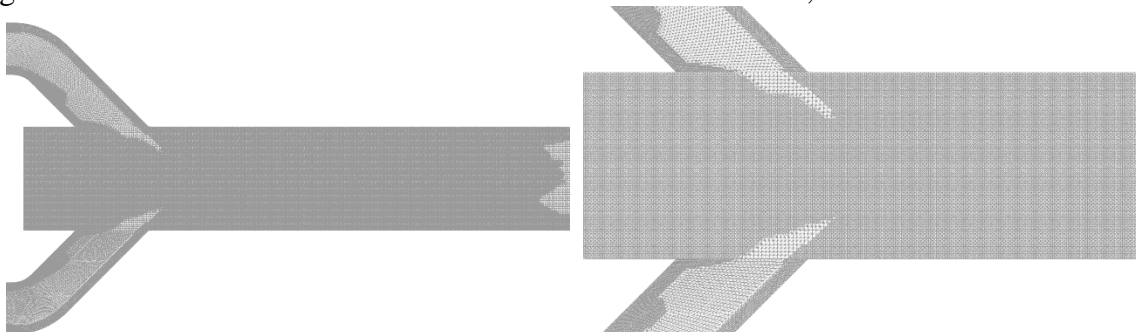


Figure 9: The computational mesh using two degrees of zoom, showing increased mesh resolution at the air inlet walls and rear of combustor.

4.2 LES Results

The simulations for the four cases all use the same procedure, starting with simulating each case on the coarse mesh (same mesh for all four cases, 2.25 million cells) until each case has converged. In general, this meant that each case ran for approximately 0.05 to 0.1 second. These results are then mapped onto the fine mesh (12.7 million cells) and the cases run until they have converged. After this the simulations are continued to sample mean data. These final mean-sampling simulations ran for approximately 0.8 seconds for the WD2, Z66 and Z87 cases, while the SD case only ran for approximately 0.3 seconds due to a significantly higher computational cost.

Figure 10 shows volumetric renderings of the instantaneous fuel and heat release for the Z87 case. The majority of the heat release is located downstream of the air jets entering the combustor, in the region between the jet and the wall. This continues downstream for approximately one third of the combustor length. The heat release is present in thin sheets, and is highly dynamic, due to the turbulent flow. The fuel jets are clearly visible entering at the head end of the combustor, but are rapidly dispersed and broken down into smaller hydrocarbons prior to the entrance of the air jets. It is important to note that this is an isolated snapshot of the highly dynamic flame, which occasionally moves far upstream in the combustor. In this case, the fuel jets are made significantly shorter, with increasing fuel consumption due to the high temperatures earlier in the combustor.

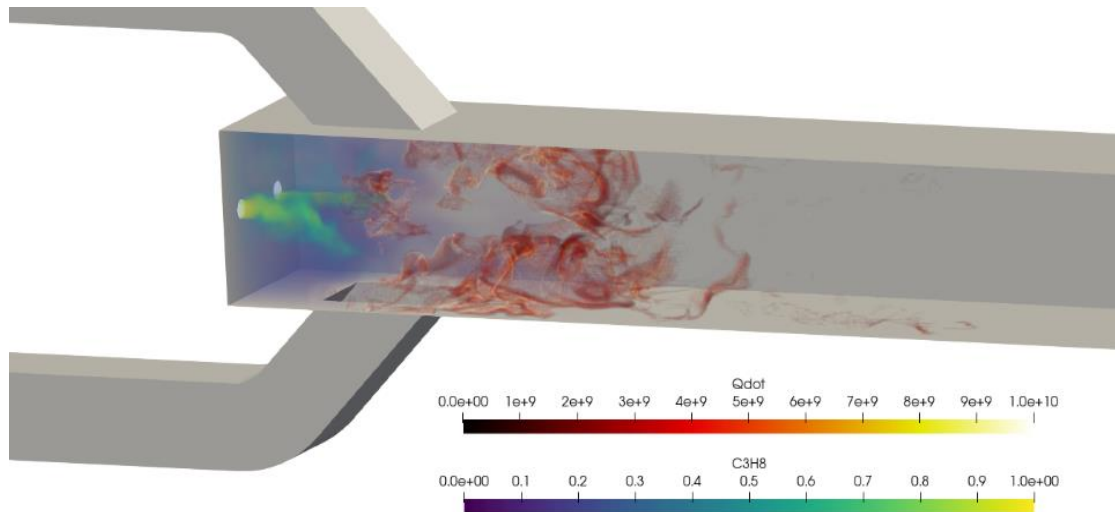


Figure 10: Volumetric rendering of instantaneous fuel concentrations and chemical heat release computed with Z87 mechanism.

Figure 11(a) shows the instantaneous coherent structures visualized using iso-surfaces of the second invariant of the rate of strain tensor, used to identify vortical structures in the flow, coloured by the instantaneous velocity. The first third of the combustor has relatively large structures, ranging from cold to hot as the combustion initiates. Immediately downstream of the air inlet, the hot larger vortex dominates the core, with surrounding colder, small-scale structures, located closer to the walls.

Figure 11(b) show streamlines of the mean velocity coloured by the mean temperature. This plot shows the four large vortices created by the incoming air flow, with one located in each quadrant of the combustor. Behind the air inlets, a recirculation zone is visible, with flow back towards the fuel injectors located around the combustor centerplane. The recirculation zones upstream of the air inlets creates spiralling vortices that connect to those produced by the air jets. After the air jets have entered the combustor and combined with the spiralling vortices the exothermic parts of the reactivity starts, forming a stable region of combustion. This region is always burning, while the flame also ignites intermittently in the upstream parts of the combustor. The downstream section of the combustor is characterized by higher velocity flow, higher temperatures and less spiralling vortices. It is in this region that the majority of the CO is converted into CO₂, hence producing a significant increase in temperature through this highly exothermic chemical process.

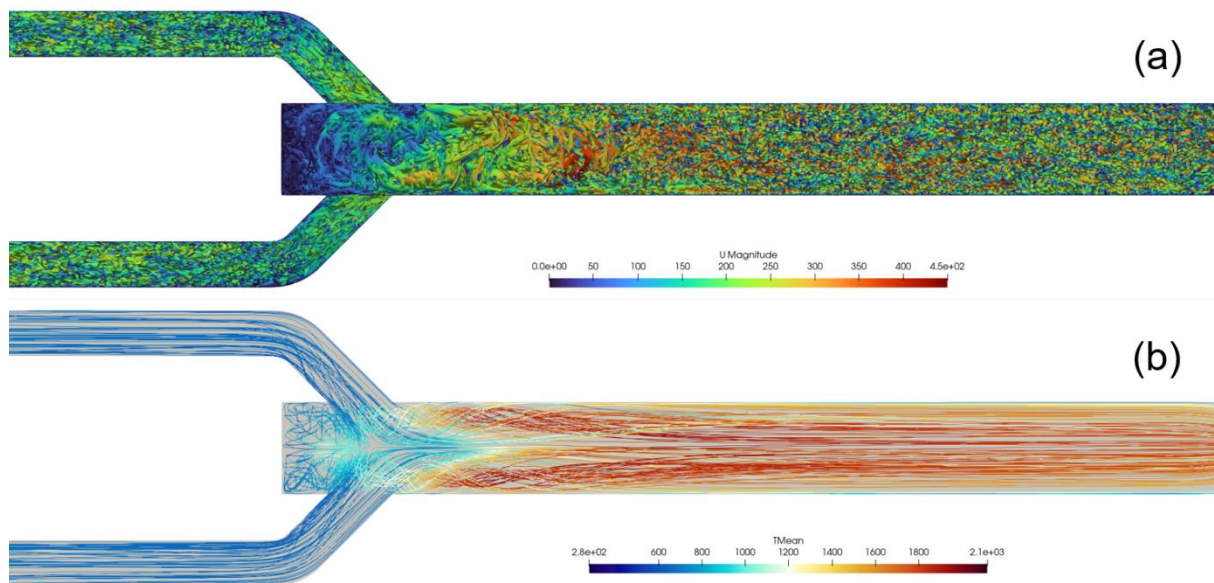


Figure 11: (a) Instantaneous coherent vortical structures for Z87 case visualized using iso-surfaces of the second invariant of the rate of strain tensor, colored by the instantaneous velocity. (b) streamlines of the mean velocity colored by the mean temperature

4.3 Comparison with experimental data

All experimental data are collected from a study by Roux et al. [6]. These consist of velocity data in axial (x) and vertical (y) directions extracted from Particle Image Velocimetry using MgO and soot particles. Of these, the axial data (U_x) is considered most descriptive and is the focus here. The experimental results together with the mean velocities extracted from the four LES cases are shown in Figure 12.

In general, all four cases match the centreline experimental data, Figure 12(a), with the only real difference being at the most upstream location where the Z87 and Z66 show reduced recirculation flow compared to SD and WD2. These schemes lie closest to the experimental data here, but only a single data point is available in this region.

Figures 12(b-d) compare the axial velocity data along three vertical centrelines at different locations along the combustor. These are located 18 mm, 120 mm and 206 mm after the air duct first entry. At the first section, $x=18$ mm in Figure 12(b), this line passes through the recirculation region and here again the Z87 and Z66 cases show the lowest recirculation with

smaller negative velocities, and lay closest to the experimental values. However, all of the mechanisms predict a larger recirculation at this point than is seen in the experiment. Further downstream, at $x = 120$ mm in Figure 12(c), the vertical sampling line is downstream of the air inlets. In the centre of the combustor, the simulated velocities all lie between the experimental results obtained, while the experiments show a faster fall-off away from the centre. Again the three larger mechanisms are closely matched, while WD2 lays furthest from the experimental data, estimating higher velocities throughout. At the most downstream location, $x = 206$ mm in Figure 12(d), all four cases predict similar velocities, all of which are higher than the experimental data. Overall, the simulated velocity results of both the centreline and the axial velocities shows that the Z66, Z87 and SD cases predict similar values, showing that the simulated velocities are relatively unaffected by the complex low-temperature chemistry and the radical species intricacies of larger mechanisms. This suggests also that there are other characteristics of the LES, such as turbulence or wall modelling, which determine the differences between the simulated and experimental velocity profiles seen here. As will be seen in the following sections, the WD2 case differs significantly compared to the other three cases regarding heat release and temperature profiles, and these differences are likely responsible for the velocity differences between the WD2 case and the other mechanisms seen here.

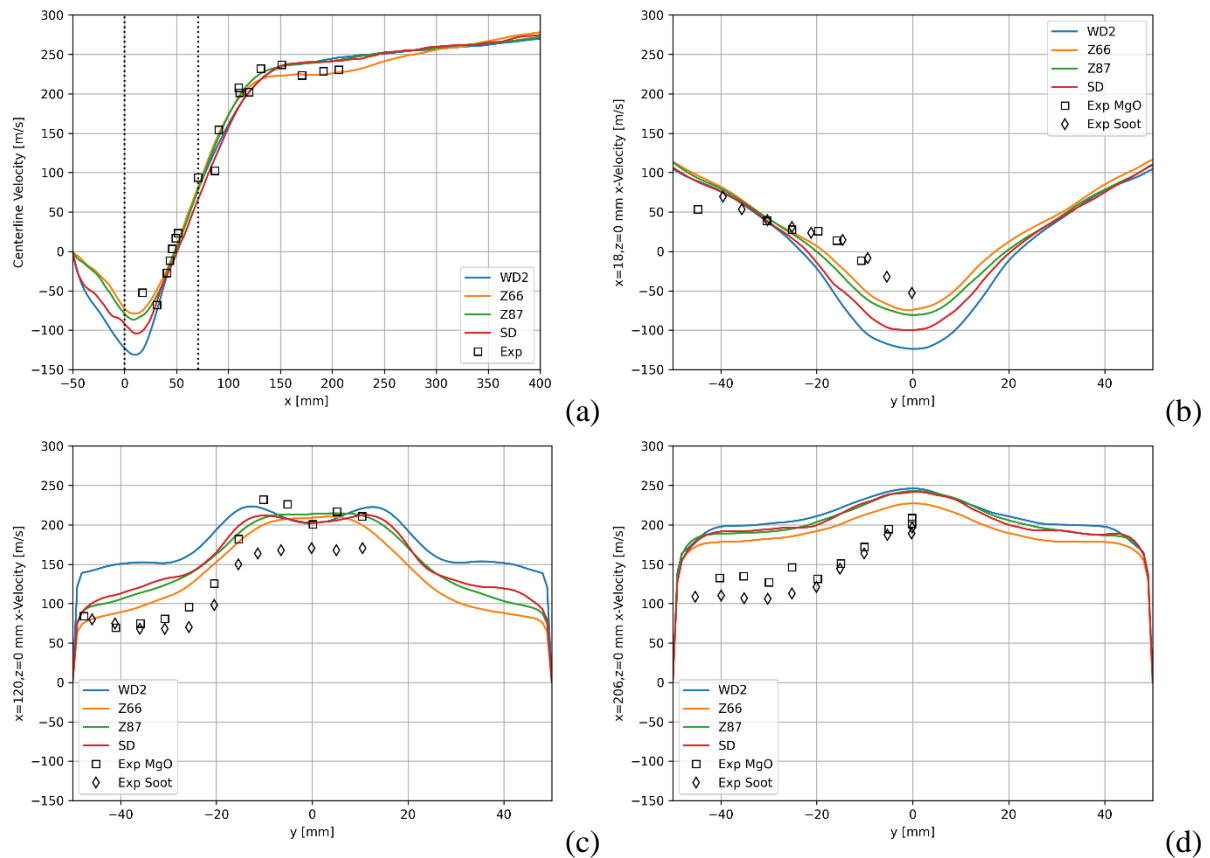


Figure 12: x -axis velocity for all four cases together with experimental data computed using MgO and soot particles. (a) $y = 0, z = 0$ axial centerline, (b-d) vertical lines with $z = 0$: (b) $x = 18$ mm, (c) $x = 120$ mm, (d) $x = 206$ mm.

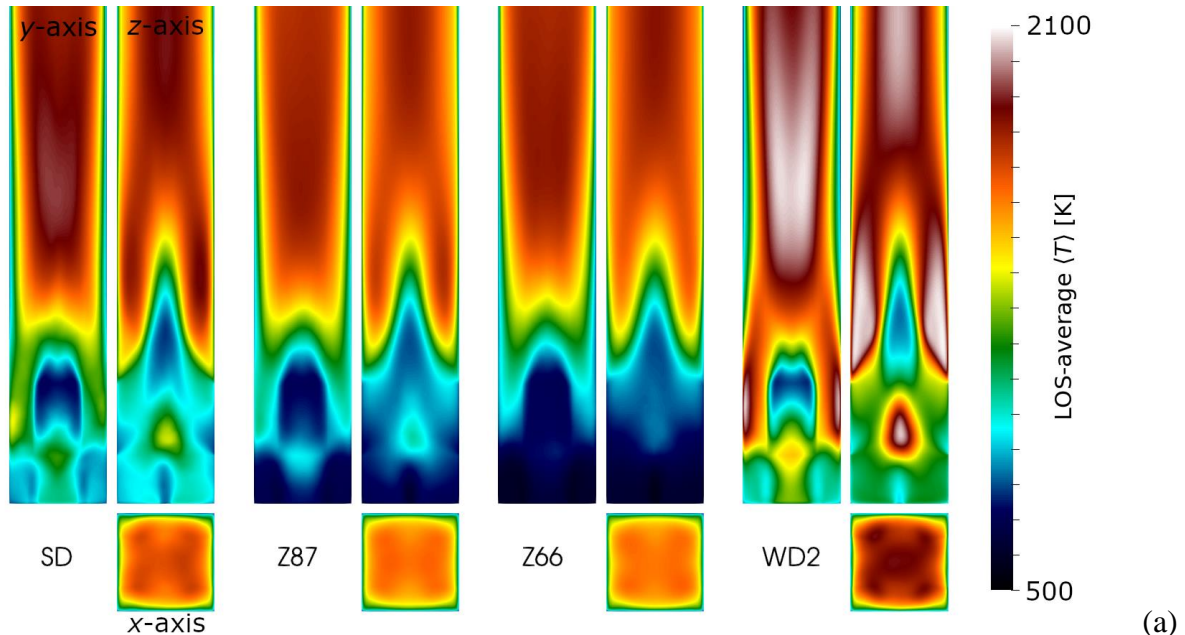
4.4 Combustion characteristics and mechanism comparisons

In order to visualize and compare the spatial distribution of the time-averaged combustion characteristics, Line-of-Sight (LoS) images are produced for the time-averaged temperature, heat release, pressure and CO mass fraction fields. These LoS images are generated by computing integral averages within the combustor along rays aligned in the x , y , and z -coordinate directions respectively. Since they are based on the temporal mean fields, they therefore represent averages over both time and space. The groups of 3 plots presented for each mechanism in Figures 13 and 14 show the LoS-averages computed along each of the x , y and z coordinate directions as indicated.

Considering first the temperature, Figure 13(a), the WD2 mechanism stands out in particular, having considerably higher temperatures in general compared to the other three mechanisms. It also shows a local high-temperature region located around the rear intersection point of the two incoming airflows. This increased temperature region is also present for the SD and Z87 cases, although with considerably lower mean temperatures. The SD, Z87 and Z66 cases all show similar behaviours downstream of the air inlets, but differ in the temperature obtained to the sides and ahead of these.

Similar trends are also seen for the heat release, Figure 13(b), where again the WD2 case stands out with considerably higher values upstream of the air inlet streams. The other three mechanisms consistently show a more distributed heat release, primarily located downstream of and to the sides of the air inlets. In particular, the x -axis integrated heat-release shows that for the SD, Z87 and Z66 mechanisms, the majority of the heat release occurs near the walls of the combustor, while with WD2 this takes place in the interior.

Both for the temperatures and heat releases there is a correlation between low ignition delay times and the intensities in upstream combustion levels, indicating that the modelling capacities of the mechanisms highly affect the upstream dynamics in the combustor.



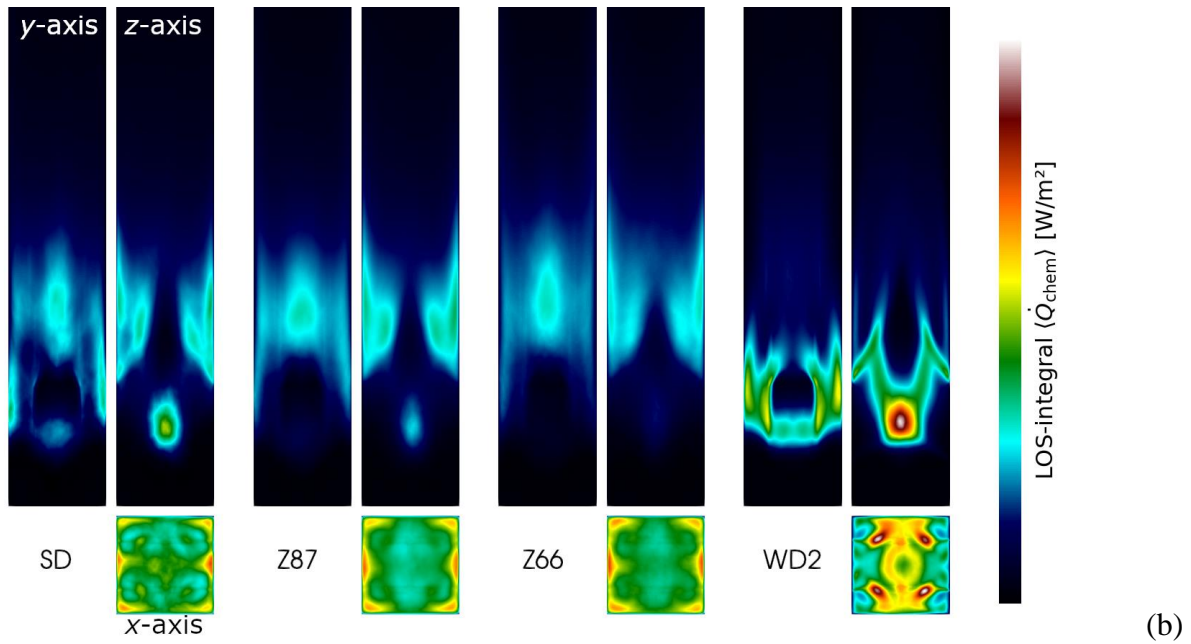


Figure 13: x, y, and z-aligned Line-of-Sight (LoS) images for all four mechanisms . (a) LoS- and time-averaged temperature, (b) LoS- and time-averaged chemical heat release.

Figure 14(a) shows LoS images for the average pressures, with the SD and Z87 cases being the most closely matched, with highly similar pressure distributions. The Z66 and WD2 cases both have a high-pressure region in the side view LoS, located around an axial position where the air inlets are placed.

Finally, CO mass fractions are plotted in Figure 14(b), showing significant differences between the four cases. Here the SD case stands out with considerable higher CO mass fractions upstream, close to the fuel inlets. The upstream part of the combustor is a region that is characterized by rich, low-temperature reaction with complex carbon-intensive reaction pathways. Of the four mechanisms used here, the SD mechanism is the only one with a large number of reaction pathways describing this regime, with several of them resulting in CO formation. The CO is however not oxidized into CO_2 until further downstream, where a significant increase in OH enables such conversion via the reaction $CO + OH \rightarrow CO_2 + H$. Closest to the SD case in terms of CO mass fractions is the Z87 case, even though the peak in CO in the upstream section is significantly below that of the SD case. The WD2 shows the lowest CO mass fractions up until $x = 0.4$, with concentrations significantly below those in the other three cases. The reason for this is the simple nature of the WD2 mechanism where all fuel is converted into CO and then directly into CO_2 , completely ignoring the complex reaction pathways of propane and initial fuel radicals such as C_3H_6 and C_2H_4 .

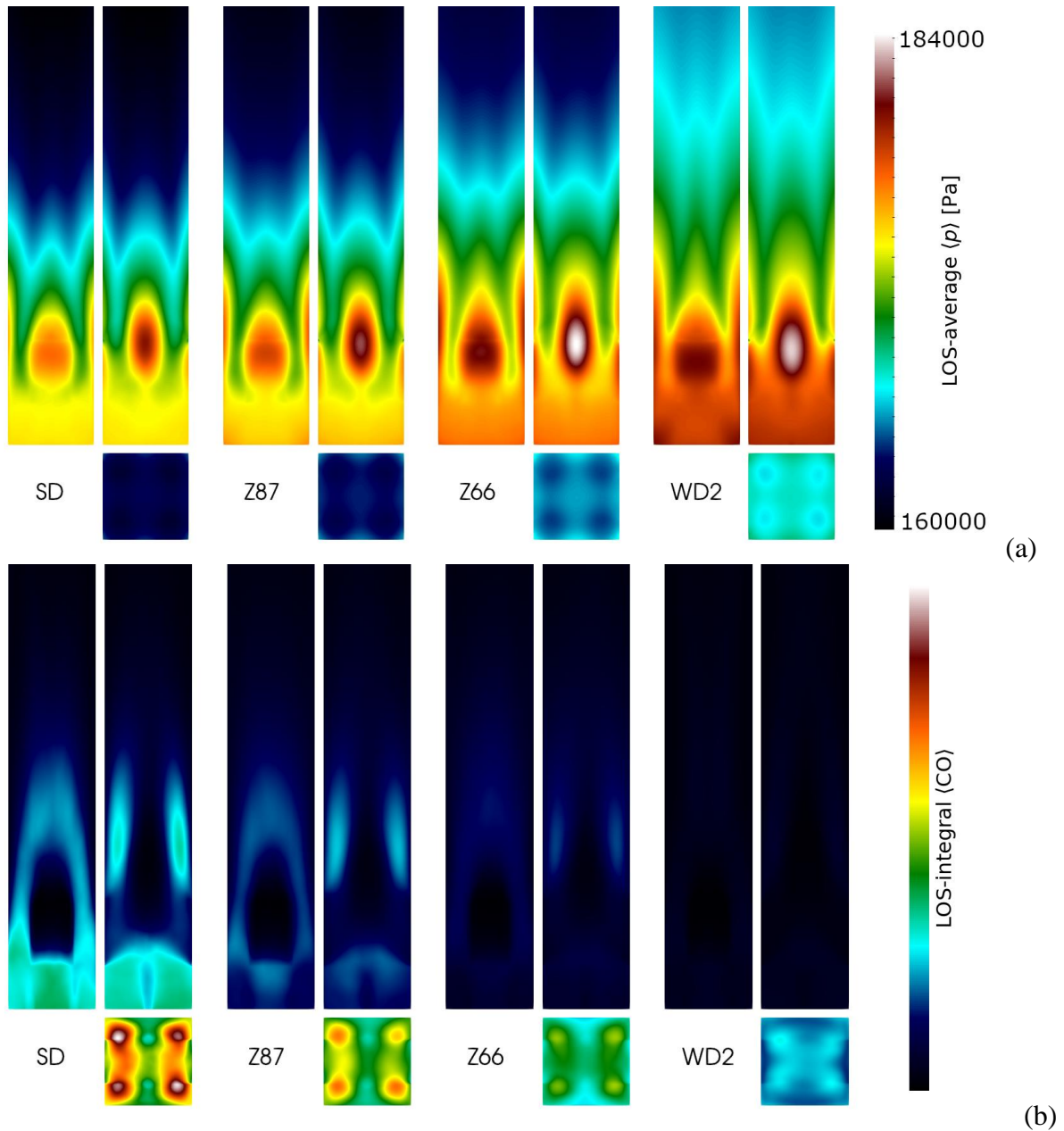


Figure 14: x, y, and z-aligned Line-of-Sight (LoS) images for all four mechanisms . (a) LoS- and time-averaged pressure, (b) LoS- and time-averaged CO fractions.

4.5 Integrated quantities versus axial distance

Presented next are comparisons of various flow quantities versus axial distance of the combustor, using integral averages over the width and height of the combustor. Figure 15, plotting the temperature for the four cases, shows significant differences for all four mechanisms, especially in the upstream section of the combustor. Firstly, the WD2 case has the highest temperature throughout the combustor. It also has a significantly elevated temperature in the upstream section of the combustor, reaching temperatures in excess of 1400 K shortly downstream of the air inlet. The short ignition delay of the WD2 chemistry, together with the overall nature of global mechanisms, means that a rapid heat release and a

high temperature is to be expected. The slowest igniting mechanism, Z66, is least likely to have a flame in this upstream region, resulting in the lowest average temperature near the injectors. The Z87 mechanism with its low-temperature chemistry included means that the flame is more often present in the upstream location compared to the Z66 mechanism, and the results of this is a slightly higher upstream temperature. Also, improved CO₂ chemistry of the Z87 mechanism compared to Z66 means that a lower peak temperature is present throughout the combustor. Finally, the SD case show a downstream temperature curve similar to Z87 but with a higher peak in the upstream section, indicating the present of a flame more of the time.

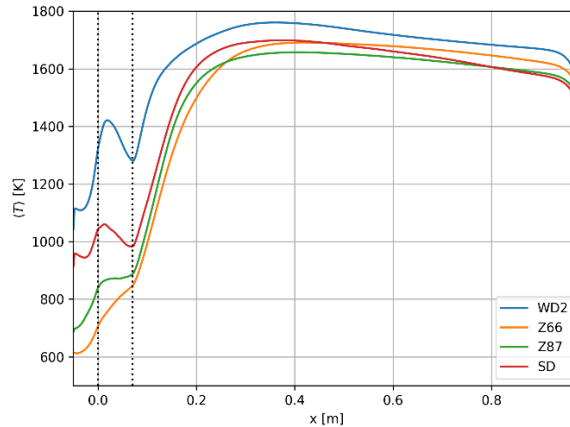


Figure 15: Cross-sectional and time-averaged temperature versus axial distance. The black dotted lines represent the location of the air duct inlets.

Figure 16(a) shows the cross-section integrated time-averaged heat release versus axial distance. The fast-igniting WD2 mechanism, with its clear and stable flame in the upstream section of the combustor, results in a high heat release concurrent with the air-inlet ducts, at $x < 0.1$ m. The almost instant burning predicted by the WD2 mechanism means that the heat release, and hence the flame anchoring point, is present considerably ahead of the other three cases. For the slowest igniting mechanism, Z66, the peak in heat release occurs at a considerable upstream location compared to the WD2 case, and the Z66 case also has a heat release slightly further downstream compared to the Z87 and SD cases. The Z87 case is similar to the Z66 case but with a narrower region of heat release, and a slightly increased level at the most upstream location. The heat release of the SD case has a similar shape and location compared to Z87, but with an early peak in the upstream section.

For the cross-section averaged pressure curves, Figure 16(b), the WD2 case has the overall highest pressures and SD the lowest, with Z87 and SD being closely matched. All four pressure curves show similar curve shapes, with differences only in their amplitudes.

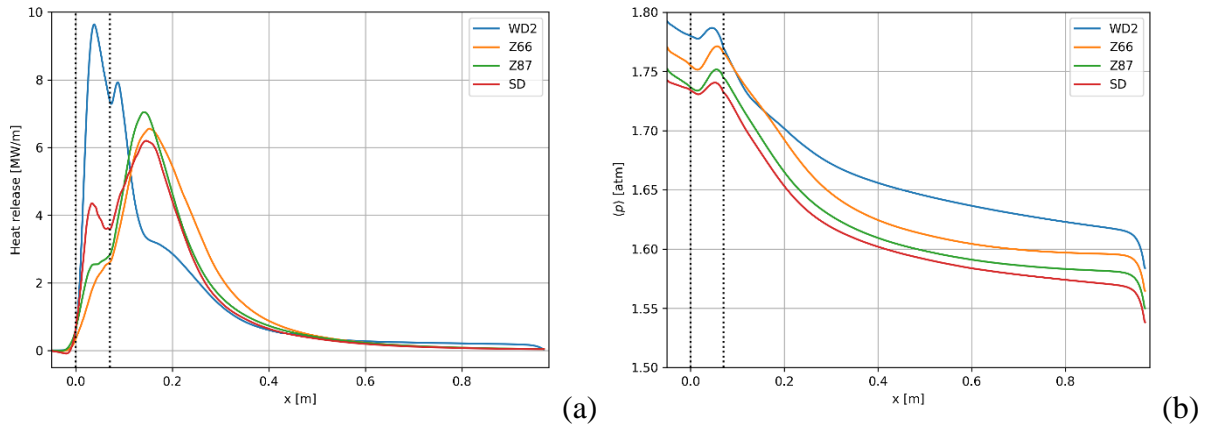


Figure 16: Cross-sectional integrated heat release versus axial distance in (a), and cross-sectional averaged pressure versus axial distance in (b). The black dotted lines indicate the location of the air duct inlets.

Figure 17 shows the integrated CO and CO₂ mass fractions versus axial distance. For CO in Figure 17(a), the SD case has by far the highest mass fractions, with especially high values upstream of the air inlets. This behaviour is also seen in the LoS images in Figure 17(b), and is due to the locally higher fuel rich sections in this part of the combustor and the accompanying reaction pathways for fuel rich conditions that are present in the SD mechanism compared to the other three.

The CO₂ profiles in Figure 17(b) show that the WD2 case has considerably higher CO₂ mass fractions throughout the combustor. This in turn correlates to the temperature curve in Figure 15 due to the highly exothermic state when moving from CO to CO₂. The remaining mechanisms show very similar CO₂ fractions downstream of the air inlets, though the SD case again shows increased CO₂ upstream of the inlets compared to the other two. The higher concentrations of both CO and CO₂ in the head end of the combustor for the SD mechanism combined with relatively low heat release here suggests that more combustion products are being drawn back into the head of the combustor by the recirculating flow for this case.

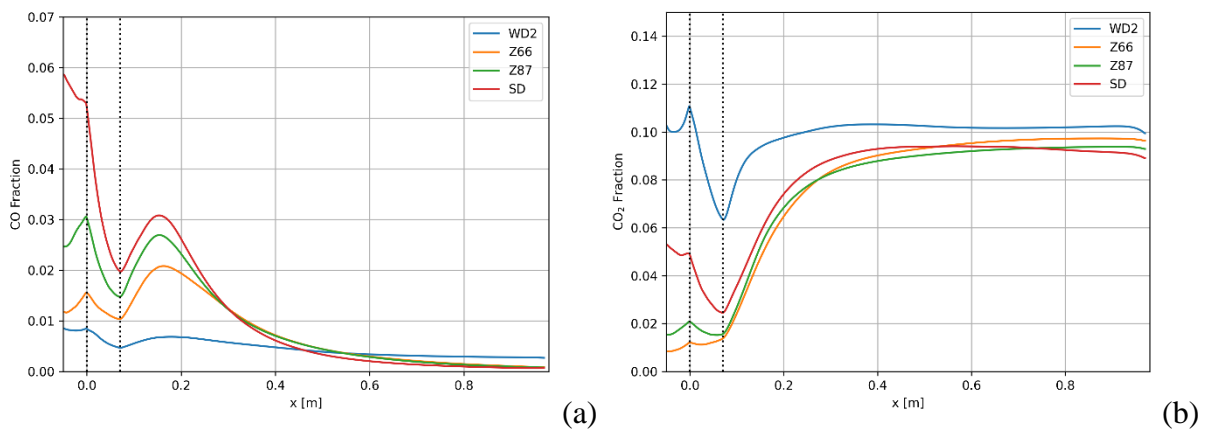


Figure 17: Integrated CO versus axial distance in (a), and CO₂ versus axial distance in (b). Both figures use values integrated over the width and height of the combustor. The black dotted lines indicate the location of the air inlets.

Conclusions

In this study a novel reduced reaction mechanism for propane-air combustion is presented, called Z87. It build on a previous mechanism but is extended to also include low-temperature chemistry. It captures the laminar flame speeds, ignition delay times and flame temperature, for a wide range of initial gas temperature and pressures, and equivalence ratios. Its compact size keeps the computational cost to a minimum and enables its use in finite rate combustion LES. It is compared against a set of experimental data, and simulation results from global, reduced and detailed reaction mechanisms. Z87 together with three of these mechanisms are then used when simulating the Ducted Rocket combustor,

The use of the mechanisms in LES simulations shows that the chemistry can have a significant effect on the heat release and species distributions within a practical ramjet-type combustor. The chemistry also was seen to have an impact on the overall flow, in particular between the global and detailed mechanisms.

In general, the Z87 reduced mechanism demonstrated improved agreement with the reference SD mechanism compared to those that did not include low-temperature kinetics, suggesting that the inclusion of low-temperature chemistry modelling plays an important role when capturing the flame characteristics and flame anchoring point. However, there are still some discrepancies between the results. In particular, the high concentrations of CO obtained at the head end of the combustor using SD were not reproduced by any of the other mechanisms and the reason for this requires further investigation.

References

- [1] Saghafian, A., Shunn, L., Philips, D. A., & Ham, F. *Large Eddy Simulations of the HIFiRE Scramjet using a Compressible Flamelet/Progress Variable Approach*. Proc Combust Inst. 2015;35:2163.
- [2] Glassman I, Yetter RA. *Combustion*. 4th ed. Elsevier; 2010.
- [3] Ristori, A., Heid, G., Brossard, C., & Bresson, A. *Characterization of the reacting two-phase flow inside a research ramjet combustor*. ONERA; 2003.
- [4] Ristori, A., Heid, G., Cochet, A., & Lavergne, G. *Experimental and numerical study of turbulent flow inside a research SDR combustor*. In Los Angeles, CA, USA; 1999. p. 2814.
- [5] Gicquel, L. Y. M., & Roux, A. *LES to ease understanding of complex unsteady combustion features of ramjet burners*. Flow Turbul Combust. 2011;(87):449–72.
- [6] Roux, A., Gicquel, L. Y. M., Sommerer, Y., & Poinso, T. J. *Large eddy simulation of mean and oscillating flow in a side-dump ramjet combustor*. Combust. Flame. 2008;152(1–2):154–76.
- [7] Zettervall, N. *Methodology for developing reduced reaction mechanisms, and their use in combustion simulations* Doctoral Dissertation, Lund University; 2021.
- [8] Zettervall, N., Nordin-Bates, K., Nilsson, E. J. K., & Fureby, C. *Large Eddy Simulation of a premixed bluff body stabilized flame using global and skeletal reaction mechanisms*. Combust Flame. 2017;179:1–22.
- [9] Zettervall, N., Fureby, C., & Nilsson, E. J. K. *Small Skeletal Kinetic Reaction Mechanism for Ethylene–Air Combustion*. Energy Fuels. 2017;31(12):14138–49.
- [10] Zettervall, N. *Reduced Chemical Kinetic Reaction Mechanism for JP-10-Air Combustion*. Energy Fuels. 2020;34(12):16624–35.
- [11] Zettervall, N., Fureby, C., & Nilsson, E. J. K. *A reduced chemical kinetic reaction mechanism for kerosene-air combustion*. Fuel. 2020;269:117446.

- [12] Zettervall, N., & Nilsson, E. J. *Semi-global Chemical Kinetic Mechanism for FAME Combustion Modeling*. Combust Sci. Technol. 2023;1–18.
- [13] Zettervall, N., Fureby, C., & Nilsson, E. J. *Reduced Chemical Kinetic Reaction Mechanism for Dimethyl Ether-Air Combustion*. Fuels. 2021;2(3):323–44.
- [14] Zettervall, N., Fureby, C., & Nilsson, E. J. K. *Small skeletal kinetic mechanism for kerosene combustion*. Energy Fuels. 2016;30(11):9801–13.
- [15] Curran, H. J., Gaffuri, P., Pitz, W. J., & Westbrook, C. K. *A comprehensive modeling study of iso-octane oxidation*. Combust Flame. 2002;129(3):253–80.
- [16] Curran, H. J., Gaffuri, P., Pitz, W. J., & Westbrook, C. K. *A comprehensive modeling study of n-heptane oxidation*. Combust Flame. 1998;114(2):149–77.
- [17] Westbrook, C. K., & Dryer, F. L. *Simplified reaction mechanisms for the oxidation of hydrocarbon fuels in flames*. Combust Sci Technol. 1981;27(1):31–43.
- [18] <http://combustion.ucsd.edu> [Internet]. *Chemical-Kinetic Mechanisms for Combustion Applications*, San Diego Mechanism web page, Mechanical and Aerospace Engineering, University of California at San Diego.
- [19] C-W. Zhou, Y. Li, U. Burke, C. Banyon, K.P. Somers, S. Khan, J.W. Hargis, T. Sikes, E.L. Petersen, M. AlAbbad, A. Farooq, Y. Pan, Y. Zhang, Z. Huang, J. Lopez, Z. Loparo, S.S. Vasu, H.J. Curran. *An experimental and chemical kinetic modeling study of 1,3-butadiene combustion: Ignition delay time and laminar flame speed measurements*. Combust Flame. 2018;197:423–38.
- [20] Fuller, M. E., Mousse-Rayaleh, A., Chaumeix, N., & Goldsmith, C. F. *Laminar flame speeds and ignition delay times for isopropyl nitrate and propane blends*. Combust Flame. 2022;242:112187.
- [21] Vagelopoulos, C. M., & Egolfopoulos, F. N. *Direct experimental determination of laminar flame speeds*. Symp Int Combust. 1998;27(1):513–9.
- [22] Vagelopoulos, C. M., Egolfopoulos, F. N., & Law, C. K. *Further considerations on the determination of laminar flame speeds with the counterflow twin-flame technique*. Symp Int Combust. 1994;25(1):1341–7.
- [23] Lowry, W., de Vries, J., Krejci, M., Petersen, E., Serinyel, Z., Metcalfe, W., & Bourque, G. *Laminar flame speed measurements and modeling of pure alkanes and alkane blends at elevated pressures*. J Eng Gas Turbines Power. 2011;133(9).
- [24] Zhao, Z., Kazakov, A., Li, J., & Dryer, F. L. *The initial temperature and N₂ dilution effect on the laminar flame speed of propane/air*. Combust Sci Technol. 2004;176(10):1705–23.
- [25] Jomaas, G., Zheng, X. L., Zhu, D. L., & Law, C. K. *Experimental Determination of Counterflow Ignition Temperatures and Laminar Flame Speeds of C₂–C₃ Hydrocarbons at Atmospheric and Elevated Pressures*. Proc Combust Inst. 2005;30(1):193–200.
- [26] Osorio, C., Morones, A., Hargis, J. W., Petersen, E. L., & Mannan, M. S. *Effect of C₂H₅F and C₃H₇F on methane and propane ignition and laminar flame speed: experimental and numerical evaluation*. J Loss Prev Process Ind. 2017;48:21–31.
- [27] Hassan, M. I., Aung, K. T., Kwon, O. C., & Faeth, G. M. *Properties of Laminar Premixed Hydrocarbon/Air Flames at Various Pressures*. J Propuls Power. 1998;14:479.
- [28] Mathieu, O., Goulier, J., Gourmel, F., Mannan, M. S., Chaumeix, N., & Petersen, E. L. *Experimental study of the effect of CF₃I addition on the ignition delay time and laminar flame speed of methane, ethylene, and propane*. Proc Combust Inst. 2015;35(3):2731–9.
- [29] Gokulakrishnan, P., Fuller, C. C., Klassen, M. S., Joklik, R. G., Kochar, Y. N., Vaden, S. N., ... & Seitzman, J. M. *Experiments and modeling of propane combustion with vitiation*. Combust Flame. 2014;161(8):2038–53.
- [30] Zhang, J., Hu, E., Zhang, Z., Pan, L., & Huang, Z. *Comparative study on ignition delay times of C₁–C₄ alkanes*. Energy Fuels. 2013;27(6):3480–7.
- [31] Tang, C., Man, X., Wei, L., Pan, L., & Huang, Z. *Further study on the ignition delay times of propane–hydrogen–oxygen–argon mixtures: Effect of equivalence ratio*. Combust Flame. 2013;160(11):2283–90.
- [32] Lam, K. Y., Hong, Z., Davidson, D. F., & Hanson, R. K. *Shock tube ignition delay time measurements in propane/O₂/argon mixtures at near-constant-volume conditions*. Proc Combust Inst. 2011;33(1):251–8.

- [33] Lamoureux, N., Paillard, C. E., & Vaslier, V. *Low hydrocarbon mixtures ignition delay times investigation behind reflected shock waves*. Shock Waves. 2002;11:309–22.
- [34] Burnett, M. A., Daniels, C., Wei, L., Wooldridge, M. S., & Wang, Z. *A computational and experimental study of the effects of thermal boundary layers and negative coefficient chemistry on propane ignition delay times*. Combust Flame. 2023;257:112415.
- [35] Molana, M., Piehl, J. A., & Samimi-Abianeh, O. *Rapid compression machine ignition delay time measurements under near-constant pressure conditions*. Energy Fuels. 2020;34(9):11417–28.
- [36] Hu, E., Zhang, Z., Pan, L., Zhang, J., & Huang, Z. *Experimental and modeling study on ignition delay times of dimethyl ether/propane/oxygen/argon mixtures at 20 bar*. Energy Fuels. 2013;27(7):4007–13.
- [37] Ramalingam, A., Fenard, Y., & Heufer, A. *Ignition delay time and species measurement in a rapid compression machine: A case study on high-pressure oxidation of propane*. Combust Flame. 2020;211:392–405.
- [38] Menon S. & Fureby C. *Computational Combustion*. In: *Encyclopedia of Aerospace Engineering*. John Wiley & Sons; 2010.
- [39] Kim, W.-W., and Menon, S. *A New Dynamic One-Equation Subgrid-Scale Model for Large Eddy Simulations*. In Reno, NV; 1995.
- [40] Sabelnikov, V., and Fureby, C. *LES Combustion Modeling for High Re Flames Using a Multi-Phase Analogy*. Combust Flame. 2013;160(1):83–96.
- [41] Nogenmyr, K. J., Fureby, C., Bai, X. S., Petersson, P., Collin, R., & Linne, M. *Large eddy simulation and laser diagnostic studies on a low swirl stratified premixed flame*. Combust Flame. 2009;156(1):25–36.
- [42] Fedina, E., & Fureby, C. *A comparative study of flamelet and finite rate chemistry LES for an axisymmetric dump combustor*. J Turbul. 2011;12(N24).
- [43] Fedina, E., Fureby, C., Bulat, G., & Meier, W. *Assessment of finite rate chemistry large eddy simulation combustion models*. Flow Turbul Combust. 2017;99(2):385–409.
- [44] Nordin-Bates, K., & Fureby, C. *Understanding scramjet combustion using LES of the HyShot II combustor: stable combustion and incipient thermal choking*. In Orlando, FL; 2015. p. 3838.
- [45] Fureby, C. *A Comparative Study of Subgrid Models, Reaction Mechanisms and Combustion Models in LES of Supersonic Combustion*. In: AIAA Propulsion and Energy 2019 Forum. 2019. p. 4273.
- [46] Weller H.G., Tabor G., Jasak H. & Fureby C. *A Tensorial Approach to CFD using Object Oriented Techniques*. Comput Phys. 1997;12(6):620–31.
- [47] Grinstein, F. F., Margolin, L. G., & Rider, W. J. *Implicit large eddy simulation. Vol. 10*. Cambridge: Cambridge university press; 2007.
- [48] Hairer, E. and Wanner, G. *Solving, O. D. E. II: Stiff and Differential-Algebraic Problems*. Berlin: Springer; 1991.